ACS OMEGA

http://pubs.acs.org/journal/acsodf

Article

Iodine Capture with Mechanically Robust Heat-Treated Ag−Al−Si−O Xerogel Sorbents

Saehwa Chong, Brian J. Riley,* Wenbin Kuang, and Matthew J. Olszta

Cite This: *ACS Omega* 2021, 6, 11628−11638

Read Online

ACCESS | Metrics & More | Article Recommendations | Supporting Information

ABSTRACT: Various radionuclides are released as gases during reprocessing of used nuclear fuel or during nuclear accidents including iodine-129 (^{129}I) and iodine-131 (^{131}I). These isotopes are of particular concern to the environment and human health as they are environmentally mobile and can cause thyroid cancer. In this work, silver-loaded heat-treated aluminosilicate xerogels (Ag-HTX) were evaluated as sorbents for iodine [$I_{2(g)}$] capture. After synthesis of the base $NaAlSiO_4$ xerogel, a heat-treatment step was performed to help increase the mechanical integrity of the $NaAlSiO_4$ gels (Na-HTX) prior to Ag-exchanging to create Ag-HTX xerogels. Samples were characterized by powder X-ray diffraction, scanning electron microscopy, energy-dispersive X-ray spectroscopy, transmission electron microscopy, Brunauer−Emmett−Teller analysis, gravimetric iodine loading, nanoindentation, and dynamic mechanical analysis. The structural and chemical analyses of Ag-HTX showed uniform distribution of Ag throughout the gel network after Ag-exchange. After $I_{2(g)}$ capture, the AgI crystallites were observed in the sorbent, verifying chemisorption as the primary iodine capture mechanism. Iodine loading of this xerogel was 0.43 g g^{-1} at 150 °C over 1 day and 0.52 g g^{-1} at 22 °C over 33 days. The specific surface area of Ag-HTX was 202 m^2 g^{-1} and decreased to 87 m^2 g^{-1} after iodine loading. The hardness of the Na-HTX was >145 times higher than that of the heat-treated aerogel of the same starting composition. The heat-treatment process increased Young's modulus (compressive) value to 40.8 MPa from 7.0 MPa of as-made xerogel, demonstrating the need for this added step in the sample preparation process. These results show that Ag-HTX is a promising sorbent for $I_{2(g)}$ capture with good iodine loading capacity and mechanical stability.

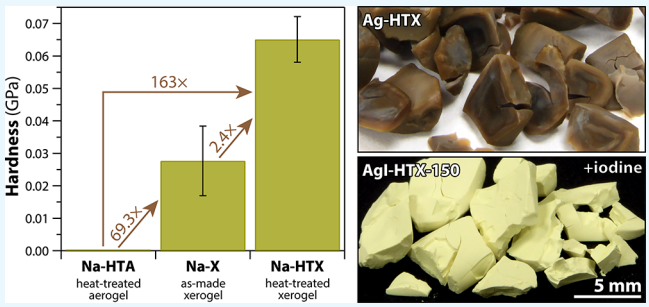

1. INTRODUCTION

Aerogels and xerogels of various compositions have been demonstrated as effective sorbents for the capture of iodine gas [i.e., $I_{2(g)}$].[1−8] Aerogels and xerogels are porous solids characterized by large specific surface areas (SSAs), high porosities, various pore sizes (s_p), small apparent densities, small indices of refraction, and low thermal conductivities.[9−15] Compared to aerogels, xerogels generally have smaller SSA, smaller porosities, smaller s_p, and larger apparent densities due to differences in the synthesis routes.[9,10,13,14] Both aerogels and xerogels are typically brought to the same alcogel stage (i.e., a solidified gel in an alcohol matrix) under identical preparation processes, but their drying processes vary.[1,4,5] Xerogels are generally synthesized through slow evaporation of the matrix solvent in the gel at a relatively low temperature (<40 °C) or at room temperature under vacuum, resulting in volume shrinkage and pore collapse by capillary forces on the pore walls. Collapse of the gel pore structure during drying can also be minimized by exchanging the solvent matrix to a nonpolar solvent (e.g., hexane) prior to the drying step.[16] In contrast to xerogels, aerogels are often synthesized using critical point drying (CPD, alternatively called supercritical drying), by which the solvent matrix is exchanged with another liquid (e.g., CO_2) that is then taken to a supercritical state by increasing the pressure and temperature of the fluid and vented as a gas to preserve the structure of the initial alcogel.[9,10,13,14] One limitation to making large quantities and sizes of aerogels using the CPD process is that an adequately sized pressure vessel (i.e., autoclave) is required to hold the sample. Alternatively, xerogels can be scaled up to various shapes and sizes with much less effort.

Table 1 summarizes the general properties and applications of some different aerogels and xerogels reported in the literature. Aerogels containing various species including carbon,[17−24] chalcogenides,[6,25,26] metal/metal oxides,[19,20,23,27,28] and organic polymers[29,30] have been synthesized and investigated in the literature. These aerogels have a wide range of applications including being used as catalysts,[12,20,21,25,27,28,31−33] cosmic dust collectors,[34,35] electro-

Received: February 16, 2021
Accepted: April 13, 2021
Published: April 23, 2021

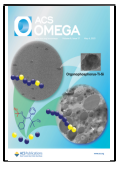

Table 1. General Properties and Applications of Some Aerogels and Xerogels[a]

gel type	composition	SSA ($m^2\ g^{-1}$)	V_p ($cm^3\ g^{-1}$)	ρ ($g\ cm^{-3}$)	application(s)	reference(s)
aerogels	SiO_2	366−1100	2.7−18	0.003−0.35	catalysis, cosmic dust capture, thermal insulation	15, 27, 31, 34, 40
	Al_2O_3	123−616	1.1−17.3	0.06−0.13	catalysis, thermal insulation	27, 31, 39
	Cr_2O_3	528−784	1.3−3.7	0.15−0.54	catalysis	27, 33
	Fe_2O_3−SiO_2	690−760	NP	NP	catalysis	41
	Fe_2O_3l$_2O_3$	230−570	2.7−13	∼0.05	catalysis	27, 42
	Al_2O_3−SiO_2	600−780	NP	0.1−0.2	thermal insulation	38
	Al_2O_3−SiO_2	96−150	0.3−0.7	NP	iodine capture	1, 5, 7
	partially sintered composite silica	11−44	NP	0.39−1.49	actinide immobilization	36
graphene aerogels	carbon	149−1100	2−4	∼0.05	catalysis, energy storage, electrode, sensor, sorbent	8, 17, 18, 20, 22, 24
	carbon + TiO_2	268, 323	0.1	NP	catalysis	20, 23
	carbon + Fe_3O_4−N	110	NP	NP	catalysis	19
	carbon + $W_{18}O_{49}$	228	0.5	0.01	catalysis	21
chalcogenide aerogels (chalcogels)	Co(Ni)−Mo(W)−S	340−528	0.7−1.2	0.19−0.3	catalysis	43
	Fe_4S_4	90−310	NP	NP	catalysis	25
	Fe−Mo−S	144	NP	NP	catalysis	44
	Co(Ni, Sb, Zn)−Mo(K, Sn)−S	240−490	NP	NP	sorbent	26
	Co-Bi(Ge, Ni)−Mo−S	127−580	0.7−3.0	NP	Tc, U, and I capture	6
xerogels	SiO_2	141−491	∼0.1	NP	optical material, medication carrier	45−47
	Pt-carbon	625−660	0.8−1.1	NP	catalysis	48
	Ag(Cu, Pd)−SiO_2	200−570	1.3−7.3	∼2.2	catalysis	49
	SnO_2	NP	NP	NP	sensor	50
	ZrO_2−SiO_2	38−115	0.2−0.4	NP	sensor	51
	analine−SiO_2	192	0.3	NP	sensor	52
	Ag−Al_2O_3−SiO_2	240	0.7	NP	iodine capture	47

[a]NP denotes "not provided". Reported densities (ρ) are apparent densities. SSA and V_p denote the specific surface area and pore volume, respectively.

des,[17,18,24] nuclear waste forms,[36] sensors,[35,37] sorbents,[1,5−7,26] and thermal insulators.[38,39]

Studies on the applications of xerogels are mostly related to their use as catalysts or sensors. Lambert et al. synthesized Pd−SiO_2, Ag−SiO_2, and Cu−SiO_2 xerogel catalysts with hierarchic textures and concluded that benzene oxidation over Ag−SiO_2 and Cu−SiO_2 xerogels and hydrodechlorination over Pd−SiO_2 xerogels are structure-insensitive reactions.[49] Later, Lambert et al. synthesized Pt-containing carbon xerogels using electrostatic adsorption and demonstrated these to be catalysts for active hydrogenation of benzene into cyclohexane.[48] Hong et al. synthesized a silica xerogel thin film with a low dielectric constant and a high-temperature limit that can be used as an intermetallic dielectric in microelectronics.[46,47] Alfaya et al. showed that ZrO_2−SiO_2 xerogels adsorb Cr(VI) and can be used as a potentiometric sensor.[51] Pavan et al. synthesized an electrode with Congo red containing aniline-SiO_2 xerogels and used these in sensor applications for ascorbic acid.[52] Lei et al. synthesized SnO_2 nanocrystalline xerogels to enhance the electrochemiluminescence reaction and applied it to detect SO_3^{2-}.[50]

Both aerogels and xerogels can be used as sorbents to capture gaseous iodine released during used nuclear fuel reprocessing.[1,5−7] Iodine-129 (^{129}I) has a long half-life ($t_{1/2}$ = 1.57×10^7 years) and iodine-131 (^{131}I) has a short $t_{1/2}$ (8.04 days), where both are mobile in the environment within the air and in groundwater, so radioiodine capture and immobilization are of great concern in nuclear waste management. Studies have shown that aerogels built with chalcogenides,[6,26] graphene,[8] composites from metal-organic-frameworks/cellulose[53] as well as both Ag-containing aerogels[1,7,8] and xerogels[1] are efficient sorbents to capture iodine. Silver as a getter metal is attractive due to its high affinity with iodine, strong chemisorption to form AgI,[5] low iodine release during consolidation (i.e., AgI has a high boiling temperature >1500 °C), and the high chemical durability of AgI.[54,55]

In a previous study,[1] a direct comparison between Ag-loaded aluminosilicate aerogels and xerogels for iodine capture showed that aerogels were more effective in capturing iodine but not substantially better than xerogels. For both aerogels and xerogels, the pore structures of the gels undergo collapse and shrinkage during Ag-exchange and iodine loading. While the as-made xerogels had a lower SSA than the as-made aerogels (i.e., 530 $m^2\ g^{-1}$ vs 600 $m^2\ g^{-1}$, respectively), the SSA values of the Ag-loaded xerogel and iodine-loaded Ag-xerogel were ∼2× and ∼4× higher than equivalent aerogels. Also, heat treatment of the aerogel before Ag-exchange and iodine loading helped to retain the initial pore structure (smaller decrease in SSA and pore volume, V_p) after subsequent treatments.

For the current study, Ag-loaded heat-treated xerogels (Ag-HTX) were evaluated as an alternative approach to Ag-loaded heat-treated aerogels (Ag-HTA) and Ag-loaded xerogels (Ag-X; not heat-treated) to capture $I_{2(g)}$. This approach is based on results from our previous studies.[1,5,7] Compared to aerogels, Ag-HTX sorbents have the following advantages: (1) they require an easier drying process (CPD is not required), (2) it is not necessary to actively reduce Ag^+ to Ag^0 for iodine capture, and (3) the heat-treatment process provides a product with significantly higher mechanical durability than aerogels, heat-treated aerogels, and xerogels.

https://doi.org/10.1021/acsomega.1c00852
ACS Omega 2021, 6, 11628−11638

From previous work with aerogels,[1,5,7] the heat-treatment process was shown to qualitatively improve mechanical properties of the base aerogel sorbents. The main goals of this work were to further develop the sorbent synthesis process and improve the properties of the Ag-loaded aluminosilicate gels (i.e., nominally $AgAlSiO_4$) by building off our previous advancements in this area[1,5,7] to achieve mechanically robust xerogel-based sorbents with high capacities for $I_{2(g)}$. In this study, the mechanical properties were quantified between heat-treated aerogels, xerogels, and heat-treated xerogels. These new heat-treated xerogel sorbents show great promise for Ag incorporation and subsequent iodine capture.

2. MATERIALS AND METHODS

2.1. Xerogel Synthesis. The base xerogel was synthesized using a modified method from the previous study by Riley et al.[7] Several of the process steps described below were not optimized, and it is likely that the synthesis time could be significantly reduced. Examples of potential improvements include reducing the gelation times and the number of solvent exchanges prior to xerogel synthesis. The following precursors were used as-received: ethanol (EtOH, 200 proof; Decon Labs), tetraethyl orthosilicate (TEOS, 99%; Sigma-Aldrich), acetic acid (HOAc, glacial; Sigma-Aldrich), sodium methoxide (NaOMe or $NaOCH_3$, 25% by volume in methanol or MeOH, Sigma-Aldrich; St. Louis, MO), aluminum tri-*sec*-butoxide [$Al(OBu^s)_3$; 97%; Sigma-Aldrich], isopropanol (IPA; C_3H_7OH, 100%, semiconductor-grade, VWR International; Radnor, PA), and deionized water (DIW, 18.2 MΩ cm).

For the base gel synthesis, a solution containing 7.94 mL of TEOS, 7.94 mL of EtOH, 0.635 mL of DIW, and 0.101 mL of HOAc (1:1 in volume for TEOS/EtOH, 1:1 in mole for TEOS/DIW, and 1:0.05 in mole for TEOS/HOAc), respectively, were mixed in a closed Teflon vessel using a magnetic stir bar for 6.5 h. The solution was placed in a nitrogen glovebox (M-Braun, Inc., Stratham, NH), and mixing was resumed. While stirring, 27.7 mL of IPA and 9.24 mL of $Al(OBu^s)_3$ were added sequentially and stirred for 15 h. Then, 8.05 mL of $NaOCH_3$ was slowly added into the solution and this was mixed for 3.6 h. The solution was removed from the glovebox, 2.54 mL of DIW was added, and this was mixed for 3 h. The mixed solution was cast into 4 mL polypropylene vials, the vials were capped, and these were stored for 2−3 days for gelation.

After gelation, the gels were removed from their vials, placed in a 50/50 solution of EtOH and DIW (by volume), and cut into smaller pieces of ∼5−10 mm on a side using a stainless steel scalpel. The gels sat in the 50/50 solution for 14 days to undergo aging and to remove the reaction byproducts from the gels through passive diffusion while hydrolysis processes were completed. The 50/50 solution was replaced 10 times over the course of 10 days to help remove the reaction byproducts. Then, these gels were solvent-exchanged in 100% EtOH 10 times to remove the water, again through passive diffusion, forming alcogels. Finally, to create xerogels, the alcogels were put into loosely capped 125 mL Nalgene bottles, placed in a glass vacuum desiccator at room temperature, and dried through slow evaporation over the course of 21 days until the gel mass became constant.

A portion of the as-made xerogel was heat-treated at 350 °C for 30 min in an alumina crucible to remove hydroxyl groups and hydrocarbons as well as to enhance the mechanical durability; these conditions were selected based on our previous work.[7] The heat-treated xerogel was named SGZ-11C-HTX and denoted as Na-HTX in this paper (this formulation is similar to SGZ-11 from our previous work[7]).

To Ag-exchange the Na-HTX gel, the Na-HTX granules were soaked in the $AgNO_3$ solution. Here, 14.73 g of $AgNO_3$ was dissolved in 500 mL of a 1:5 solution of MeOH and DIW (by volume) in a 1 L glass beaker (i.e., 0.17 M Ag^+ solution); masses were weighed using an analytical balance (ME204E; Mettler Toledo; ±0.1 mg). Then, 1 g of Na-HTX was added into a Teflon-mesh basket (ET8500-18P; Industrial Netting; Minneapolis, MN) and this was inserted into the solution, and the solution was stirred for 24 h; this ratio of gel mass to moles of Ag^+ (i.e., m_g/X_{cat} = 11.53 g mol^{-1}) was based on our previous work.[1,§] After soaking the gels in the $AgNO_3$ solution, the gels were removed from the solution, placed in a loosely capped glass scintillation vial, and dried in a vacuum desiccator for several days until a constant mass was observed. The Ag-loaded heat-treated xerogel was denoted as Ag-HTX. For more details on this process, such as the preparation of the Teflon-mesh baskets, see our previous work.[7]

2.2. Iodine Loading. *2.2.1. High-Temperature Iodine Uptake (150 °C).* To assess the iodine loading in the Ag-HTX sample, 0.3033 ± 0.0045 g of Ag-HTX was placed into three separate tared 4 mL glass vials (Qorpak GLC-00980), which were placed into a 1 L perfluoroalkoxy (PFA) vessel (100-1000-01; Savillex; Eden Prairie, MN) along with a 20 mL glass scintillation vial containing ∼0.9 g of solid iodine pieces (m_I, 99.999%, Alfa Aesar). Masses were obtained using the ME204E analytical balance. An additional empty vial (the blank) was added to assess the iodine capture on the vial itself. Then, the Savillex vessel was placed into an oven (3511FSQ, Isotemp, Fisher Scientific; Hampton, NH) at 150 °C (±4 °C) for 24 h. Following this soak, the vials were carefully removed from the apparatus and placed directly into the same oven at 150 °C for 1 h so that any physisorbed iodine could be desorbed. The resulting product after iodine loading was named AgI-HTX-150.

2.2.2. Room-Temperature Iodine Loading (22 °C). The iodine loading capacity for Ag-HTX was also evaluated at room temperature using a similar approach to the high-temperature iodine uptake experiments described previously. Here, the PFA vessel was loaded with a single glass vial with 0.0409 g of Ag-HTX, a single glass vial with 0.0812 g of silver mordenite (i.e., IONEX Type Ag900 AgZ), a blank vial, and a container of iodine crystals as before (∼0.9 g); the lid was added, and these were left at room temperature (∼22 °C). The AgZ was added here as it is a well-known sorbent for $I_{2(g)}$ and is used as a benchmark evaluation.[56] The mass of the gel was recorded 21 times with a minimum time interval of 1 day over 31 days of iodine exposure until a constant mass was observed. Following the iodine uptake experiment, the glass vial was removed from the PFA vessel and left in a fume hood at room temperature to allow for any physisorbed iodine to desorb. For desorption, the masses of the gels were recorded for 9 days until a constant mass was observed. This sample was named AgI-HTX-RT.

2.2.3. Iodine Loading Calculations. Following the iodine loading experiments, eqs 1−3 were used to evaluate the gravimetric iodine capacities, based on mass uptake, where m_s was the starting mass of the sample, m_{s+I} is the final mass following iodine capture, m_I was the mass of iodine captured by the sample by mass difference from m_s [eq 1], $m\%_I$ was the mass % of iodine in the final sample [eq 2], and "g g^{-1}" was the term denoting the mass of iodine captured per starting mass of

https://doi.org/10.1021/acsomega.1c00852
ACS Omega 2021, 6, 11628−11638

the sorbent (gravimetric iodine loading) [eq 3]. Finally, the Ag utilization (AgU) was calculated as the ratio of I to Ag in the iodine-sorbed gels shown in eq 4 using data collected from energy-dispersive X-ray spectroscopy (EDS) in atom % with built-in standards in the Bruker ESPRIT software. When AgU > 1, some physisorbed iodine may remain within the sample or iodine is binding to a different location within the sorbent than to the getter directly. Also, it is possible that the iodine could adsorb directly to the aerogel surface

$$m_I = m_{s+I} - m_s \quad (1)$$

$$m\%_I = 100 \times (m_I/m_{s+I}) \quad (2)$$

$$\text{I} - \text{loading} = m_I/m_s(\text{or g g}^{-1}) \quad (3)$$

$$\text{AgU} = 100 \times [\text{I}]/[\text{Ag}](\text{atom \%}) \quad (4)$$

2.3. Specific Surface Area, Pore Volume, and Pore Size. The SSA, V_p, and s_p values were measured with nitrogen [$N_{2(g)}$] adsorption and desorption isotherms collected with a Quadrasorb EVO/SI (Quantachrome Instruments, Anton Paar). Samples were broken into 1−3 mm sized pieces to fit into pre-tared borosilicate type-C long cells with a 6 mm sample chamber bulb (part number 193621, Quantachrome Instruments, Anton Paar). Sample masses were collected on the ME204E analytical balance and ranged from 0.0240 ± 0.0048 g for Na-HTX, 0.0466 ± 0.0032 g for Ag-HTX, and 0.0589 ± 0.0156 g for AgI-HTX. The samples were degassed under vacuum at 25 °C for 12 h before the adsorption measurements. For each sample, nitrogen adsorption and desorption data were collected at 77.3 K with 54 measurements over a total run time of 13−21 h. The surface area was determined using the 5-point Brunauer−Emmett−Teller (BET) method.[57] The Barrett−Joyner−Halenda (BJH) method was used for the pore volume and pore size distribution determination.[58]

2.4. Nanoindentation. A Nanovea M1 mechanical tester equipped with a standard nano-Berkovich tip was employed to perform nanoindentation on heat-treated aerogels (Na-HTA), as-made xerogel (Na-X), and Na-HTX. The Na-HTA samples are 11A gels from a previous study,[5] which were heat-treated at 350 °C for 30 min. Data for Na-X and Na-HTX were collected in triplicate, so averages and standard deviations ($\pm 1\sigma$) were calculated for these. Each sample was seated on a flat steel base, and microscopes were used for choosing indentation locations. A maximum force of 1 mN, a loading rate of 1 mN min^{-1}, an unloading rate of 1 mN min^{-1}, an approach speed of 1 μm min^{-1}, and a contact force threshold of 0.1 mN (to avoid triggering by environmental vibration) were used for testing. Load−depth curves were generated with hardness and modulus values calculated by the control software.

2.5. Dynamic Mechanical Analysis. To demonstrate the mechanical stability of the as-made and heat-treated xerogel, dynamic mechanical analysis (DMA) was performed using a TA Instruments Q800 dynamic mechanical analyzer (Figure S1) to investigate the mechanical properties, including Young's modulus and strain-at-breaking. DMA measures the whole specimen, while nanoindentation focuses on local properties in compression. The testing was performed using a compression setup under the controlled force mode. A preloading force of 0.001 N, a force track of 125%, and a frequency of 1 Hz were adopted. Each sample was previously measured in diameter and mounted into fixtures by 5 in-lb torque force. Then, the sample was pressed at room temperature by ramping the force at a rate of 0.5 N min^{-1} until breakage or a 35% diameter of displacement was reached if they did not break, during which stress and strain data were recorded.

2.6. Powder X-ray Diffraction. Powder X-ray diffraction (P-XRD) was performed by grinding samples in an agate mortar and pestle and adding these ground powders onto a 25 mm zero-background silicon holder by first suspending in isopropanol, dropping onto the holder, and allowing the isopropanol to dry prior to analysis. This process resulted in better adherence of the sample on the holder and does not appear to affect the sample diffraction based on previous experience with similar gels. In the event the isopropanol addition affects the pore structure of the gels during drying, the samples used for P-XRD analysis were not used in other characterization techniques (e.g., BET/BJH, electron microscopy). Samples were then analyzed with a D8 Advance (Bruker AXS Inc.; Madison, WI) diffractometer with Cu Kα emission. The instrument was equipped with a LynxEye position-sensitive detector with a collection window of 3° 2θ. Typical scan parameters were 10−70° 2θ with a step of 0.04° 2θ and a 2 s dwell at each step but the dwell times were increased as needed to maintain a good signal-to-noise ratio. Bruker AXS DIFFRAC^{plus} EVA (v4.1) and TOPAS (v5) software programs were used to identify and quantify the crystalline phases, respectively. Whole pattern fitting was done according to the fundamental parameter approach.[59]

2.7. Optical Pictures. Pictures were taken of the samples using a Canon Rebel T1i digital camera using Canon OES software. For getting scale bars on the images, each image was collected at the same magnification (zoom) and a ruler was included in each picture (not shown) so that a scale bar could be added to the final image composite.

2.8. Scanning Electron Microscopy and Energy-Dispersive X-ray Spectroscopy. Scanning electron microscopy (SEM) was performed on the specimens using a JSM-7001F field-emission gun microscope (JEOL USA, Inc.; Peabody, MA). For the SEM analysis, samples were adhered to a double-stick carbon tape and sputter-coated with 2.5 nm of Pt or Ir metal to create a conductive coating using an EMS 150T ES (Quorum Technologies Ltd., U.K.). The EDS was performed on the same powder mounts with a Bruker xFlash 6|60 (Bruker AXS Inc.; Madison, WI) using ESPRIT (v2.0). The conditions used for data collection were 15 kV and ∼50−80k counts s^{-1}. For EDS analysis, a minimum of 5 locations were collected, including locations on separately prepared specimens, so that averages and standard deviations could be calculated.

2.9. Transmission and Scanning Transmission Electron Microscopies and Selected Area Diffraction. Samples were prepared for transmission and scanning transmission electron microscopies (TEM and STEM, respectively) using the drop method onto lacy carbon grids. A pinhead amount of powder of each sample was placed between two glass slides, which were rubbed vigorously to further separate the powders into the smallest possible form. A lacy carbon grid was then placed onto the sheared powders to adhere the particles to the lacy carbon. Samples were analyzed in both TEM and STEM modes on a JEOL ARM200CF aberration-corrected (probe) TEM. A ≤70 μm condenser aperture was used to minimize beam damage. Selected area diffraction (SAD) was also conducted. Then, EDS spectros-

https://doi.org/10.1021/acsomega.1c00852
ACS Omega 2021, 6, 11628−11638

copy was performed in STEM mode using a JEOL Centurio detector with a collection angle of 1.9 sR.

3. RESULTS

Pictures of the heat-treated xerogels (Na-HTX), Ag-exchanged xerogels (Ag-HTX), and iodine-loaded Ag-exchanged xerogels (AgI-HTX-150) are shown in Figure 1, where appearances

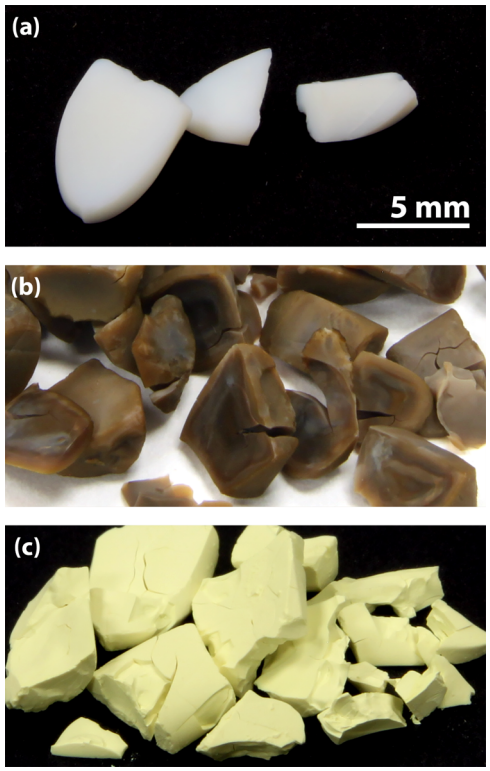

Figure 1. Pictures of (a) Na-HTX, (b) Ag-HTX, and (c) AgI-HTX-150. The scale bar is the same for all images.

were opaque white, dark brown, and bright yellow, respectively. The shrinkage between the alcogel stage (not shown) and xerogel stage was noticeable at ~30% based on rough measurements of several cylindrically shaped granules. The diameter shrinkage between the Na-X and Na-HTX stages was ~10%. Based on the pictures shown in Figure 1, it is apparent that the large granules did not significantly shrink in volume between the xerogel (Na-HTX), Ag-exchange (Ag), and iodine-loaded stages of sample preparation. It should also be noted that cracks can be observed in the Ag-HTX and AgI-HTX-150 samples, which were likely introduced to the granules during the drying process after the Ag-exchange to convert Na-HTX granules into Ag-HTX granules.

Iodine loading in AgI-HTX-150 was calculated using the gravimetric uptake measurements from three different samples of the same batch of Ag-HTX for determining the precision of the measurement (Table 2). The results showed that I-loading was 0.429 ± 0.006 g g^{-1} at 150 °C after 1 day, which was higher than the results from the previous study for both Ag-xerogel that was not heat-treated (i.e., AgI-X-150 = 0.33 g g^{-1}) and heat-treated aerogel (i.e., AgI-HTA-150 = 0.41 g g^{-1}) under the same iodine capture conditions.[1]

The room-temperature iodine loading experiment for Ag-HTX to create sample AgI-HTX-RT was investigated to understand the absorption kinetics of gaseous iodine by these

Table 2. Summary of Gravimetric Iodine Loading Data, $m_{\%I}$, and I-Loading for Ag-HTX-150 Replicates (Including Average and Standard Deviations, ±1σ), AgI-HTX-RT, and AgZ[a]

sample ID	m_s (g)	m_{s+I} (g)	m_I (g)	$m\%_I$ (mass %)	I-loading (g g^{-1})
AgI-HTX-150-1	0.2981	0.4275	0.1294	30.27	0.434
AgI-HTX-150-2	0.3058	0.4349	0.1291	29.68	0.422
AgI-HTX-150-3	0.3061	0.4384	0.1323	30.18	0.432
average	0.3033	0.4336	0.1303	30.04	0.429
SD	0.0045	0.0056	0.0018	0.31	0.006
AgI-HTX-RT	0.0409	0.0611	0.202	33.06	0.494
AgZ	0.3195	0.3613	0.0418	11.57	0.131

[a]Also, data are provided for AgI-HTX-RT; only a single data point was collected for this experiment. Data are also included for AgZ from a previous study performed under the same conditions (i.e., AgZ+I–1) from Riley et al.[7] for comparison.

sorbents. Figure 2 shows that most of the iodine uptake into Ag-HTX occurred within 20 days, and then the iodine loading

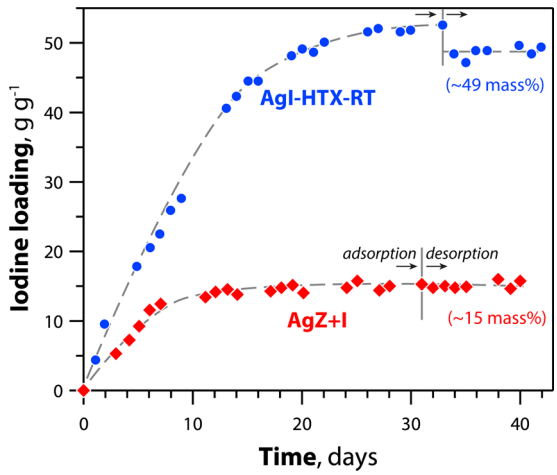

Figure 2. Iodine loading [i.e., g g^{-1}; see eq 3] of AgI-HTX-RT is compared to AgZ+I at room temperature. The Ag-mordenite (AgZ) used for this experiment is the same as that used in a previous study.[7] The vertical lines denote the time at which point the iodine was removed from the vials.

rate slowed down substantially and reached a maximum iodine loading of ~0.52 g g^{-1} after ~27 days. Compared to Ag-mordenite (AgZ+I), which reached a maximum iodine loading of ~15 mass % after 19 days, the AgI-HTX-RT sample demonstrated a 3-fold mass increase in iodine uptake over the duration of the experiment. However, the desorption plot showed that AgI-HTX-RT lost about 6 mass % of iodine, possibly due to desorption of physisorbed iodine on the pore surfaces of the sorbent. These final values equate to an iodine loading of ~0.49 g g^{-1} and are some of the highest values reported for oxide-based $I_{2(g)}$ sorbents.

Some differences were observed in the AgU [i.e., Ag utilization shown in eq 4] values for the AgI-HTX-150, AgI-HTX-RT, and AgZ + I samples. The values for AgI-HTX-150 and AgI-HTX-RT were notably different at 1.0 ± 0.1 and 1.2 ± 0.1, respectively (see Table 3). Values of AgU > 1 suggest iodine interactions in locations within the gel structure other

https://doi.org/10.1021/acsomega.1c00852
ACS Omega 2021, 6, 11628–11638

Table 3. EDS Data (Atomic %) for Na-HTX, Ag-HTX, and AgI-HTX Including Average and Standard Deviations ($\pm 1\sigma$) in Parentheses Below Each Data Point, and Standard Deviations of <0.5 Are Shown As (0)[a]

sample ID	Na	Al	Si	Ag	I	AgU	Al/Si	Si/(Na + Ag)
Na-HTX	34	33	33	-	-	-	1.01	1.0
	(1)	(0)	(1)	-	-	-	(0.03)	(0.1)
Ag-HTX	0.4	36	36	27	-	-	0.99	1.3
	(0.4)	(1)	(1)	(2)	-	-	(0.04)	(0.1)
AgI-HTX-150	0.3	28	29	21	21	1.0	0.98	1.4
	(0.5)	(1)	(1)	(1)	(1)	(0.1)	(0.03)	(0.1)
AgI-HTX-RT	0.1	28	28	20	24	1.2	0.99	1.4
	(0.3)	(1)	(1)	(1)	(1)	(0.1)	(0.02)	(0.1)

[a]Note that the data do not include oxygen as it was not quantified. See Tables S1−S3 for more information.

than with the getter (i.e., Ag in this study), but the desorption data shown in Figure 2 would suggest that this process had run to completion evidenced by the plateau of the data. The AgI-HTX-150 AgU data were closer to that of the AgZ+I (1.0 ± 0.1) and indicate nearly full utilization of the Ag active getter (see Table S5).

Several SEM micrographs and regions of EDS analysis are provided in the Supporting Information for Na-HTX (Figures S2 and S3), Ag-HTX (Figures S4−S6), AgI-HTX-150 (Figures S7−S9), AgI-HTX-RT (Figure S10), and AgZ+I (Figure S11). The EDS results summarized in Table 3 document the exchange of Na with Ag during the Ag-exchange process and incorporation of I into the structure during iodine uptake. The EDS data for the different locations of the samples are provided in Tables S1−S5. These data show that Na-HTX has a composition very close to the target of $NaAlSiO_4$. Additional calculations provided in Table 3 show how the Al/Si atomic ratio remains very close to 1 (i.e., 0.98−1.01) for all samples, whereas the Si/(Na + Ag) atomic ratio is near 1 (i.e., 0.96) for Na-HTX but 1.30 after Ag-exchanging (Ag-HTX). While the Ag does substitute for Na in the gel structure, not all of the stoichiometric Ag is added back to the gel based on the starting Na concentration, so the composition of Ag-HTX is probably closer to $Ag_{0.75}AlSiO_{3.88}$ than the target of $AgAlSiO_4$. These Si/(Na + Ag) ratios are further increased in the iodine-loaded materials, suggesting some additional volatile losses of Na or Ag during iodine loading (i.e., 1.4 for AgI-HTX-150 and AgI-HTX-RT).

Additional SEM−EDS analyses were conducted on cross-sectioned granules of Ag-HTX and AgI-HTX-150. Several granules of each sample were mounted in resin and polished using glycol-based diamond suspensions to prevent leaching of the samples into the polishing solution. The SEM−EDS collages from Ag-HTX and AgI-HTX-150 are shown in Figures S12 and S13, respectively. Figure S12 shows the even distribution of Al, Si, Ag, and O, where the brighter particles represent Ag. Figure S13 provides some additional information that has not been observed before, where the Ag and I distributions fluctuate as a function of location within the granule. In both EDS line scans, the Na level remains constant, but the other elements fluctuate. The EDS line scan in Figure S13c shows a depletion of Ag and I at the surface of the granule, but also that the levels of Ag, Al, Si, and I fluctuate, where Si and Al change inversely to Ag and I based on the location in the granule. Figure S13a,e show how the sizes of AgI crystallites change depending on the distance from the surface of the gel granule. This could be from incongruent drying rates between the surfaces and interior regions of the granules during xerogel synthesis.

Table 4 shows the changes in SSA, V_p, and s_p values of xerogel before and after Ag-exchange and iodine uptake at 150 °C; the isotherms and pore size distribution plots are provided in Figure S14. The as-made Na-HTX showed an SSA of 370 $m^2\ g^{-1}$ and a V_p of 1.83 $cm^3\ g^{-1}$, but both values decreased almost by half after Ag-impregnation and further dropped after iodine uptake at 150 °C. The substantial decreases in SSA and V_p after Ag-impregnation and iodine uptake were also observed in the previous studies.[1,7] The s_p values from both adsorption and desorption indicate the variation of pore sizes covering the range of mesopores to macropores.

Table 4. Summary of BET and BJH Analyses Including Specific Surface Area (SSA), Pore Volume (V_p), Pore Size on Adsorption ($s_{p,ads}$), and Pore Size on Desorption ($s_{p,des}$)[a]

sample ID	SSA ($m^2\ g^{-1}$)	V_p ($cm^3\ g^{-1}$)	$s_{p,ads}$ (nm)	$s_{p,des}$ (nm)
Na-HTX	370 (8)	1.83 (0.03)	6−60	8−32
Ag-HTX	202 (8)	0.98 (0.05)	6−60	13−32
AgI-HTX	87 (5)	0.48 (0.04)	6−60	13−32

[a]Since these samples were run in triplicate, standard deviations ($\pm 1\sigma$) are provided in parentheses for SSA and V_p values.

The P-XRD pattern of Na-HTX showed an amorphous structure as expected from the previous studies (Figure 3).[1,7,9,10] The Ag^0 and AgI phases were also observed after Ag-exchange and iodine uptake, respectively. The peak

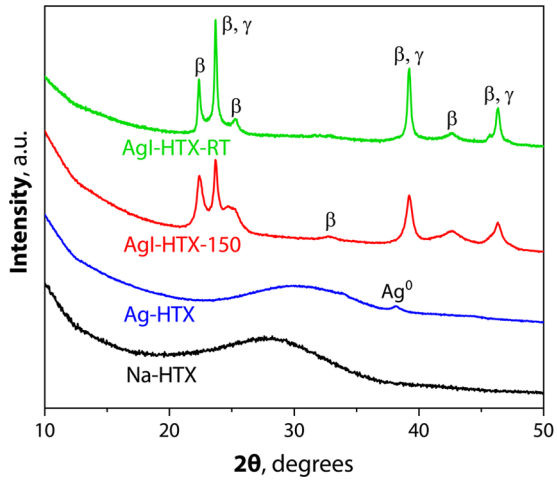

Figure 3. P-XRD patterns of Na-HTX, Ag-HTX, AgI-HTX-150, and AgI-HTX-RT with crystalline phases including Ag^0 (ICSD 670299), β denoting β-AgI (ICSD 62790), and γ denoting γ-AgI (ICSD 61542). ICSD is the Inorganic Crystal Structure Database.

https://doi.org/10.1021/acsomega.1c00852
ACS Omega 2021, 6, 11628−11638

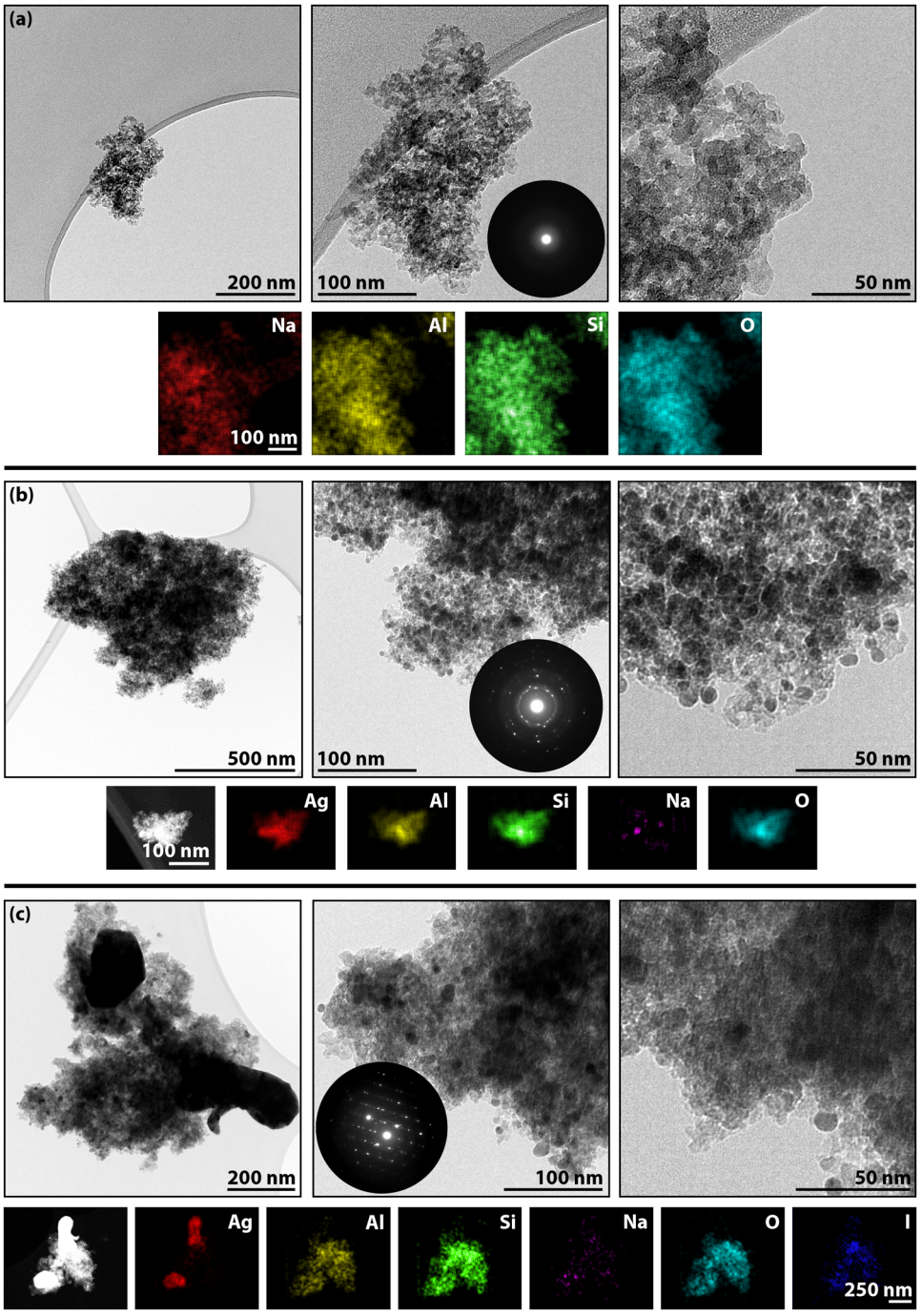

Figure 4. Summary of TEM micrographs (increasing magnification from left to right), SAD patterns (insets in the middle TEM micrographs), and STEM−EDS elemental maps for (a) Na-HTX, (b) Ag-HTX, and (c) AgI-HTX-150.

intensity of the Ag^0 phase was relatively small, and the crystallite size determination with the Rietveld method was inadequate. In the previous study,[1] Ag^0 was observed without applying any active reduction of Ag^+ incorporated into the gel matrix during Ag-exchanging and this is also the case in the current study. The passive reduction of Ag^+ to Ag^0 is possibly due to carboreduction under vacuum with residual carbon from the alkoxides used to build the gel network or from residual hydrocarbon solvents (e.g., EtOH, isopropanol).

Collages are provided in Figure 4 for TEM/SAD and STEM/EDS results for Na-HTX (Figure 4a), Ag-HTX (Figure 4b), and AgI-HTX-150 (Figure 4c). For each set of TEM micrographs, three separate magnifications are provided. In agreement with P-XRD results shown in Figure 3, the SAD pattern of Na-HTX shows diffuse rings that indicate the amorphous network. The STEM−EDS collage for Na-HTX in Figure 4a shows the uniformly distributed elements, which form the gel network. For Ag-HTX (Figure 4b), the SAD pattern shows the diffraction spots indicative of crystalline Ag^0, and the STEM−EDS collage shows homogeneously distributed Ag particles within the Ag-HTX; the low signal of Na corroborates the very low values measured during SEM−EDS analysis (Table 3). The TEM micrographs of AgI-HTX-150 (Figure 4c) show both large, dark AgI crystals and some

https://doi.org/10.1021/acsomega.1c00852
ACS Omega 2021, 6, 11628−11638

smaller AgI crystals; the SAD pattern shows diffraction spots indicative of crystalline AgI. Similarly, the uniform distribution of iodine in STEM−EDS maps shows that gaseous iodine was captured efficiently through the whole structure; darker spots more concentrated in Ag were observed suggesting more densely packed Ag regions (e.g., agglomerations of Ag^0 nanoparticles).

Table 5 summarizes the nanoindentation results for hardness and modulus. These results showed that the hardness of Na-HTX was ~2.4-fold higher than that of the as-made xerogel (i.e., Na-X) and >145-fold higher than that of heat-treated aerogel (Na-HTA) from our previous study (Figure 5).[1] Dynamic mechanical analysis showed that Young's moduli for Na-X and Na-HTX were 7.0 and 40.8, with strain-at-breaking values of 7.02 and >1.76%, respectively (Figure 6). Considering the similarity in structural parameters between aerogels and xerogels, the relatively high hardness of the xerogels is one of the significant advantages from the perspective of engineering robust sorbents for industrial applications.

Table 5. Summary of Nanoindentation Measurements (Hardness and Modulus) on Heat-Treated Aerogels, Xerogels, and Heat-Treated Xerogels[a]

sample	hardness (GPa)	modulus (GPa)
Na-HTA	0.0004	0.014
Na-X	0.0277	0.476
	(0.0107)	(0.115)
Na-HTX	0.0651	0.634
	(0.0070)	(0.158)

[a]Since replicates were run on the Na-X and Na-HTX, standard deviations ($\pm 1\sigma$) are provided in parentheses below each data point.

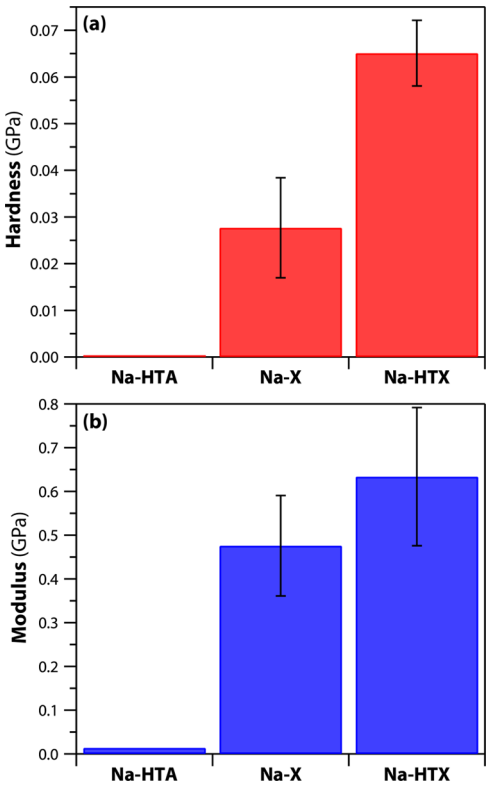

Figure 5. Comparison of (a) hardness and (b) modulus data collected from nanoindentation analysis on Na-HTA, Na-X, and Na-HTX. The error bars for Na-X and Na-HTX data series are the standard deviations from Table 5.

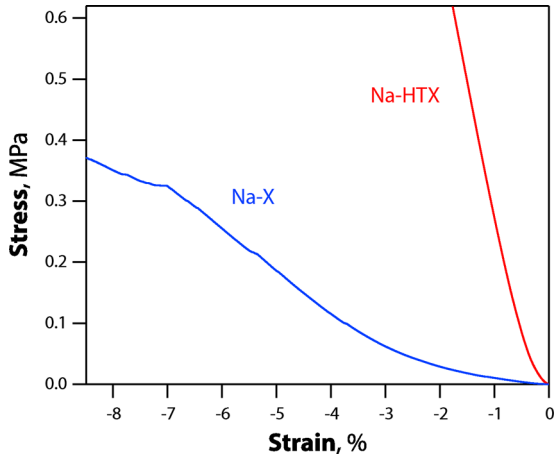

Figure 6. Dynamic mechanical analysis results for as-made xerogels (Na-X) and heat-treated xerogels (Na-HTX).

4. DISCUSSION

In our original study published in 2017,[7] several different parameters were evaluated for synthesizing aluminosilicate gels, including many with Na and a target as-batched composition of $NaAlSiO_4$. However, it was often observed that aerogels made from these compounds had Na concentrations lower than the targeted atomic ratios with Al and Si (i.e., Al/Na = 1.4, Si/Na > 1.76 for NAS-11a-AM). In a more recent study from 2020,[1] it was observed for the first time in our work that the compositions of aerogels (i.e., 12bA) and xerogels (i.e., 12bX) made from the same alcogel batch were compositionally different. The EDS data showed a composition for the xerogels being very close to the Na/Al/Si target molar ratio of 1:1:1 (i.e., 1.03:1.00:0.96), whereas the equivalent ratios for the aerogel were notably different at 0.66:1:00:1.26. The conclusion drawn from these comparisons is that gel compositions can vary based on the preparation process, but the only real difference between the synthesis of aerogels and xerogels from the same batch of alcogels is the CPD process used when making aerogels. It is believed that the CPD process can sometimes change the composition of the final aerogel and this is possibly due to the solubility of certain gel components in liquid and/or supercritical CO_2 (i.e., Na > Al > Si).

In the original study from 2017,[7] several other aspects of these gels were evaluated including Ag loading under different conditions, adjusting the redox chemistry of the added Ag atoms, as well as the iodine loading. Originally, it was thought that some sort of chemical tether would be needed to bind the Ag to the gel matrix, but after initial testing, it was discovered that the Na in the gel matrix could be replaced with Ag on a near 1:1 molar basis. After this discovery, the process of binding Ag^+ to the gels was evaluated in a fairly substantial process to determine several things including (1) the optimum soak time (t_s) required to exchange Na^+ for Ag^+ at a $[Ag^+]$ concentration of 0.1734 M (i.e., t = 1−90 min), (2) the optimum $[Ag^+]$ at a fixed 90 min soak time (i.e., $[Ag^+]$ = 0.0217−0.1734 M), (3) the effect of adding thiol (i.e., −SH) tethers using (3-mercaptopropyl)trimethoxysilane before soaking gels in $AgNO_3$ solution to help bind the Ag^+ to the gel

https://doi.org/10.1021/acsomega.1c00852
ACS Omega 2021, 6, 11628−11638

network,[2,3] and (4) evaluating the difference between only adding Ag^+ and reducing the Ag^+ to Ag^0 under H_2/Ar. The data showed that full Na → Ag exchange could be obtained at the max [Ag^+] evaluated of 0.1734 M after 90 min of soaking. It was also observed that the −SH tethers were not required to install Ag in the gel and adding these −SH tethers only decreased the Ag loading and also introduced unwanted organic molecules to the gel network. Finally, it was determined that the iodine capture performance of Ag-loaded aerogels was similar no matter if the Ag^+ was actively reduced to Ag^0 or not actively reduced (where some Ag^0 was still observed; see Figure 3). All of these developments helped simplify the synthesis process implemented in the current study. Some additional steps were included in the 2017 study[7] to evaluate the Ag-exchange capacity if no Na were present in the base gel. These data showed that Ag could be loaded onto pure aluminosilicate aerogels but at a much lower concentration, which resulted in much lower iodine capacities; thus, these materials were abandoned for further study.

The current study was a logical next step following these previous studies.[1,5,7] The heat-treatment process for $NaAlSiO_4$ aerogels was demonstrated to drastically reduce the loss in SSA and pore volume following the Ag-exchange process.[1] However, the xerogels retained higher percentages of the original SSA (+10%) and pore volume (+15%) after Ag-exchange compared to heat-treated aerogels, so they were the topic of the current study. The heat-treated xerogels in the current study (Na-HTX) had a lower SSA (i.e., 370 ± 8 m^2 g^{-1}) than as-made xerogels (Na-X) from the previous study (530 m^2 g^{-1}),[1] and this is attributed to the heat-treatment step (i.e., 350 °C, 30 min) used to strengthen the xerogel network before the BET measurements were collected. The SSA of the Na-HTX is still very high for xerogels. These two gels were batched using different solvents and sodium alkoxides, and this could have also played a role in the differences in the final properties of the materials.

Another main difference in the current work from our previous work is that mechanical testing was conducted on the Na-HTX to compare these data with those from Na-HTA and Na-X. The DMA results exhibit how the mechanical rigidity of the base xerogel can be greatly enhanced by a simple heat-treatment process. However, this heat-treatment process decreases SSA and V_p values and could potentially reduce the iodine loading capacity, even if only slightly, as was demonstrated for aerogels in our previous study.[1] Thus, the heat-treatment process can be considered when more mechanically durable sorbent is needed for specific applications.

The final difference in this study was the evaluation of $I_{2(g)}$ capture at both room temperature and at 150 °C. The gravimetric iodine loading capacities were different at 0.429 ± 0.006 and 0.494 g g^{-1} for AgI-HTX-150 and AgI-HTX-RT, respectively. The differences between these values are notable, and the causes for this difference are unknown; this could be partly due to physisorbed iodine on the AgI-HTX-RT sample that was not removed prior to EDS analysis based on the lower temperature desorption step. This shows the utility of these sorbents for capturing $I_{2(g)}$ under different conditions. Investigating the relationship between SSA and iodine loading capacities revealed no direct relationships. From the data collected across these sorbents, it appears that the SSA in the starting sorbent has little impact on the $I_{2(g)}$ sorption capacities. However, all structural parameters including SSA, V_p, and s_p as well as the distribution of Ag^0 crystallites in the structure might affect the iodine loading capacities, and further investigation is warranted to better understand the relationship.

5. SUMMARY AND CONCLUSIONS

In this study, heat-treated Ag-loaded xerogels were evaluated as iodine sorbents at room temperature and at 150 °C with iodine capacities of 0.429 ± 0.006 and 0.494 g g^{-1} for AgI-HTX-150 and AgI-HTX-RT, respectively. The I-loading capacity of the Ag-containing heat-treated xerogel (Ag-HTX) was 3 times higher than that of AgZ at room temperature and was similar to Ag-containing heat-treated aerogel (Ag-HTA) at 150 °C. The SSA of the Na-HTX (base heat-treated xerogel) in this study was close to that of the heat-treated aerogel (Na-HTA) from our previous study (370 m^2 g^{-1} vs 420 m^2 g^{-1}). Nanoindentation and dynamic mechanical analysis were used to compare the hardness, modulus, and strain-at-breaking for heat-treated aerogels, xerogels, and heat-treated xerogels. The results showed that the hardness of the heat-treated xerogel was >145-fold higher than that of the heat-treated aerogel of the same composition. Also, heat-treating the xerogels increased the modulus to 40.8 from 7.0 MPa for the as-made xerogel. These improvements demonstrate the utility of a simple heat treatment of 350 °C for 30 min before Ag-exchanging to further increase the mechanical integrity of the sorbent. Several simplifications were made to similar sorbents from previous studies, and additional optimizations could be made to further unlock the potential of these sorbents. These results show that Ag-loaded heat-treated xerogels are a promising sorbent for the capture of $I_{2(g)}$ and should be further explored in the future.

■ ASSOCIATED CONTENT

Supporting Information

The Supporting Information is available free of charge at https://pubs.acs.org/doi/10.1021/acsomega.1c00852.

SEM and EDS data, BET/BJH data, and pictures of the mechanical testing apparatus (PDF)

■ AUTHOR INFORMATION

Corresponding Author

Brian J. Riley − *Pacific Northwest National Laboratory, Richland, Washington 99354, United States;* orcid.org/0000-0002-7745-6730; Phone: (509)372-4651; Email: brian.riley@pnnl.gov

Authors

Saehwa Chong − *Pacific Northwest National Laboratory, Richland, Washington 99354, United States*

Wenbin Kuang − *Pacific Northwest National Laboratory, Richland, Washington 99354, United States*

Matthew J. Olszta − *Pacific Northwest National Laboratory, Richland, Washington 99354, United States*

Complete contact information is available at: https://pubs.acs.org/10.1021/acsomega.1c00852

Author Contributions

The manuscript was written through contributions of all authors. All authors have given approval to the final version of the manuscript.

Funding

This work was funded by the Department of Energy Office of Nuclear Energy.

Notes

The authors declare no competing financial interest.

■ ACKNOWLEDGMENTS

Pacific Northwest National Laboratory (PNNL) is operated by Battelle Memorial Institute for the DOE under contract DE-AC05-76RL01830. The authors are thankful to Ken Marsden and James King for programmatic support and Shari Li for help with the BET measurements. The authors thank Jared Kroll and Jacob Peterson for their help in developing the sol−gel synthesis procedure for the original base materials used in this study.

■ REFERENCES

(1) Chong, S.; Riley, B. J.; Peterson, J.; Olszta, M. J.; Nelson, Z. Gaseous iodine sorbents: A comparison between Ag-loaded aerogel and xerogel scaffolds. *ACS Appl. Mater. Interfaces* **2020**, *12*, 26127−26136.

(2) Matyáš, J.; Fryxell, G. E.; Busche, B. J.; Wallace, K.; Fifield, L. S. Functionalized silica aerogels: Advanced materials to capture and immobilize radioactive iodine. In *Ceramic Materials for Energy Applications: Ceramic Engineering and Science Proceedings*; Lin, H.-T.; Katoh, Y.; Fox, K. M.; Belharouak, I.; Widjaja, S.; Singh, D., Eds.; Wiley—The American Ceramic Society: Daytona Beach, FL, 2011; Vol. *32*, pp 23−33.

(3) Matyáš, J.; Ilton, E. S.; Kovařík, L. Silver-functionalized silica aerogel: Towards an understanding of aging on iodine sorption performance. *RSC Adv.* **2018**, *8*, 31843−31852.

(4) Riley, B. J.; Chong, S. Environmental remediation with functional aerogels and xerogels. *Global Challenges* **2020**, *4*, No. 2000013.

(5) Riley, B. J.; Chong, S.; Olszta, M. J.; Peterson, J. A. Evaluation of getter metals in Na−Al−Si−O aerogels and xerogels for the capture of iodine gas. *ACS Appl. Mater. Interfaces* **2020**, *12*, 19682−19692.

(6) Riley, B. J.; Chun, J.; Um, W.; Lepry, W. C.; Matyas, J.; Olszta, M. J.; Li, X.; Polychronopoulou, K.; Kanatzidis, M. G. Chalcogen-based aerogels as sorbents for radionuclide remediation. *Environ. Sci. Technol.* **2013**, *47*, 7540−7547.

(7) Riley, B. J.; Kroll, J. O.; Peterson, J. A.; Matyáš, J.; Olszta, M. J.; Li, X.; Vienna, J. D. Silver-loaded aluminosilicate aerogels as iodine sorbents. *ACS Appl. Mater. Interfaces* **2017**, *9*, 32907−32919.

(8) Scott, S. M.; Hu, T.; Yao, T.; Xin, G.; Lian, J. Graphene-based sorbents for iodine-129 capture and sequestration. *Carbon* **2015**, *90*, 1−8.

(9) Gesser, H. D.; Goswami, P. C. Aerogels and related porous materials. *Chem. Rev.* **1989**, *89*, 765−788.

(10) Pierre, A. C.; Pajonk, G. M. Chemistry of aerogels and their applications. *Chem. Rev.* **2002**, *102*, 4243−4266.

(11) Du, A.; Zhou, B.; Zhang, Z.; Shen, J. A special material or a new state of matter: A review and reconsideration of the aerogel. *Materials* **2013**, *6*, 941−968.

(12) Fricke, J.; Emmerling, A. Aerogels—Preparation, Properties, Applications. In*Chemistry, Spectroscopy and Applications of Sol−Gel Glasses*; Springer, 1992; pp 37−87.

(13) Hüsing, N.; Schubert, U. Aerogels—Airy materials: chemistry, structure, and properties. *Angew. Chem., Int. Ed.* **1998**, *37*, 22−45.

(14) Tokudome, Y.; Nakanishi, K.; Kanamori, K.; Fujita, K.; Akamatsu, H.; Hanada, T. Structural characterization of hierarchically porous alumina aerogel and xerogel monoliths. *J. Colloid Interface Sci.* **2009**, *338*, 506−513.

(15) Dorcheh, A. S.; Abbasi, M. H. Silica aerogel: Synthesis, properties and characterization. *J. Mater. Process. Technol.* **2008**, *199*, 10−26.

(16) Sigel, G. A.; Domszy, R. C. Xerogels and their preparation. U.S. Patent US6156223A2000.

(17) Reynolds, G. A. M.; Fung, A. W. P.; Wang, Z. H.; Dresselhaus, M. S.; Pekala, R. W. The effects of external conditions on the internal structure of carbon aerogels. *J. Non-Cryst. Solids* **1995**, *188*, 27−33.

(18) Worsley, M. A.; Pauzauskie, P. J.; Olson, T. Y.; Biener, J.; Satcher, J. H., Jr.; Baumann, T. F. Synthesis of graphene aerogel with high electrical conductivity. *J. Am. Chem. Soc.* **2010**, *132*, 14067−14069.

(19) Wu, Z.-S.; Yang, S.; Sun, Y.; Parvez, K.; Feng, X.; Müllen, K. 3D nitrogen-doped graphene aerogel-supported Fe_3O_4 nanoparticles as efficient electrocatalysts for the oxygen reduction reaction. *J. Am. Chem. Soc.* **2012**, *134*, 9082−9085.

(20) Zhang, Z.; Xiao, F.; Guo, Y.; Wang, S.; Liu, Y. One-pot self-assembled three-dimensional TiO_2-graphene hydrogel with improved adsorption capacities and photocatalytic and electrochemical activities. *ACS Appl. Mater. Interfaces* **2013**, *5*, 2227−2233.

(21) Li, X.; Yang, S.; Sun, J.; He, P.; Xu, X.; Ding, G. Tungsten oxide nanowire-reduced graphene oxide aerogel for high-efficiency visible light photocatalysis. *Carbon* **2014**, *78*, 38−48.

(22) Zhu, C.; Han, T. Y.-J.; Duoss, E. B.; Golobic, A. M.; Kuntz, J. D.; Spadaccini, C. M.; Worsley, M. A. Highly compressible 3D periodic graphene aerogel microlattices. *Nat. Commun.* **2015**, *6*, No. 6962.

(23) Li, Y.; Cui, W.; Liu, L.; Zong, R.; Yao, W.; Liang, Y.; Zhu, Y. Removal of Cr(VI) by 3D TiO_2-graphene hydrogel via adsorption enriched with photocatalytic reduction. *Appl. Catal., B* **2016**, *199*, 412−423.

(24) Fung, A. W. P.; Wang, Z. H.; Lu, K.; Dresselhaus, M. S.; Pekala, R. W. Characterization of carbon aerogels by transport measurements. *J. Mater. Res.* **1993**, *8*, 1875−1885.

(25) Shim, Y.; Yuhas, B. D.; Dyar, S. M.; Smeigh, A. L.; Douvalis, A. P.; Wasielewski, M. R.; Kanatzidis, M. G. Tunable biomimetic chalcogels with Fe_4S_4 cores and $[Sn_nS_{2n+2}]^{4-}$ (n = 1, 2, 4) building blocks for solar fuel catalysis. *J. Am. Chem. Soc.* **2013**, *135*, 2330−2337.

(26) Subrahmanyam, K. S.; Sarma, D.; Malliakas, C. D.; Polychronopoulou, K.; Riley, B. J.; Pierce, D. A.; Chun, J.; Kanatzidis, M. G. Chalcogenide aerogels as sorbents for radioactive iodine. *Chem. Mater.* **2015**, *27*, 2619−2626.

(27) Pajonk, G. M. Aerogel catalysts. *Appl. Catal.* **1991**, *72*, 217−266.

(28) Cauqui, M. A.; Rodriguez-Izquierdo, J. M. Application of the sol-gel methods to catalyst preparation. *J. Non-Cryst. Solids* **1992**, *147−148*, 724−738.

(29) Boday, D. J.; Stover, R. J.; Muriithi, B.; Keller, M. W.; Wertz, J. T.; DeFriend Obrey, K. A.; Loy, D. A. Strong, low-density nanocomposites by chemical vapor deposition and polymerization of cyanoacrylates on aminated silica aerogels. *ACS Appl. Mater. Interfaces* **2009**, *1*, 1364−1369.

(30) Tao, Y.; Endo, M.; Kaneko, K. A review of synthesis and nanopore structures of organic polymer aerogels and carbon aerogels. *Recent Pat. Eng.* **2008**, *1*, 192−200.

(31) Teichner, S. J.; Nicolaon, G. A.; Vicarini, M. A.; Gardes, G. E. E. Inorganic oxide aerogels. *Adv. Colloid Interface Sci.* **1976**, *5*, 245−273.

(32) Ward, D. A.; Ko, E. I. Preparing catalytic materials by the sol-gel method. *Ind. Eng. Chem. Res.* **1995**, *34*, 421−433.

(33) Armor, J. N.; Carlson, E. J.; Conner, W. C., Jr. Synthesis of high surface area chromium(III) oxides. *React. Solids* **1987**, *33*, 155−159.

(34) Tsou, P. Silica aerogel captures cosmic dust intact. *J. Non-Cryst. Solids* **1995**, *186*, 415−427.

(35) Hrubesh, L. W. Aerogel applications. *J. Non-Cryst. Solids* **1998**, *225*, 335−342.

(36) Reynes, J.; Woignier, T.; Phalippou, J. Permeability measurement in composite aerogels: application to nuclear waste storage. *J. Non-Cryst. Solids* **2001**, *285*, 323−327.

(37) Venkateswara Rao, A.; Haranath, D.; Pajonk, G. M.; Wagh, P. B. Optimisation of supercritical drying parameters for transparent

silica aerogel window applications. *Mater. Sci. Technol.* **1998**, *14*, 1194−1199.
(38) Hurwitz, F. I.; Gallagher, M.; Olin, T. C.; Shave, M. K.; Ittes, M. A.; Olafson, K. N.; Fields, M. G.; Guo, H.; Rogers, R. B. Optimization of alumina and aluminosilicate aerogel structure for high-temperature performance. *Int. J. Appl. Glass Sci.* **2014**, *5*, 276−286.
(39) Wang, W.; Zhang, Z.; Zu, G.; Shen, J.; Zou, L.; Lian, Y.; Liu, B.; Zhang, F. Trimethylethoxysilane-modified super heat-resistant alumina aerogels for high-temperature thermal insulation and adsorption applications. *RSC Adv.* **2014**, *4*, 54864−54871.
(40) Reim, M.; Körner, W.; Manara, J.; Korder, S.; Arduini-Schuster, M.; Ebert, H. P.; Fricke, J. Silica aerogel granulate material for thermal insulation and daylighting. *Sol. Energy* **2005**, *79*, 131−139.
(41) Blanchard, F.; Pommier, B.; Reymond, J.; Teichner, S. New Fischer−Tropsch catalysts of the aerogel type. In *Studies in Surface Science and Catalysis*; Elsevier, 1983; Vol. *16*, pp 395−407.
(42) Li, H.; Legros, R.; Brereton, C. M. H.; Grace, J. R.; Chaouki, J. Hydrodynamic behaviour of aerogel powders in high-velocity fluidized beds. *Powder Technol.* **1990**, *60*, 121−129.
(43) Bag, S.; Gaudette, A. F.; Bussell, M. E.; Kanatzidis, M. G. Spongy chalcogels of non-platinum metals act as effective hydrodesulfurization catalysts. *Nat. Chem.* **2009**, *1*, 217−224.
(44) Yuhas, B. D.; Smeigh, A. L.; Douvalis, A. P.; Wasielewski, M. R.; Kanatzidis, M. G. Photocatalytic hydrogen evolution from FeMoS-based biomimetic chalcogels. *J. Am. Chem. Soc.* **2012**, *134*, 10353−10356.
(45) Ahola, M.; Kortesuo, P.; Kangasniemi, I.; Kiesvaara, J.; Yli-Urpo, A. Silica xerogel carrier material for controlled release of toremifene citrate. *Int. J. Pharm.* **2000**, *195*, 219−227.
(46) Hong, J.-K.; Yang, H.-S.; Jo, M.-H.; Park, H.-H.; Choi, S.-Y. Preparation and characterization of porous silica xerogel film for low dielectric application. *Thin Solid Films* **1997**, *308*−*309*, 495−500.
(47) Hong, J.-K.; Kim, H.-R.; Park, H.-H. The effect of sol viscosity on the sol−gel derived low density SiO_2 xerogel film for intermetal dielectric application. *Thin Solid Films* **1998**, *332*, 449−454.
(48) Lambert, S.; Job, N.; D'Souza, L.; Pereira, M. F. R.; Pirard, R.; Heinrichs, B.; Figueiredo, J. L.; Pirard, J.-P.; Regalbuto, J. R. Synthesis of very highly dispersed platinum catalysts supported on carbon xerogels by the strong electrostatic adsorption method. *J. Catal.* **2009**, *261*, 23−33.
(49) Lambert, S.; Cellier, C.; Grange, P.; Pirard, J.-P.; Heinrichs, B. Synthesis of Pd/SiO_2, Ag/SiO_2, and Cu/SiO_2 cogelled xerogel catalysts: Study of metal dispersion and catalytic activityCatalysts: Study Of Metal Dispersion And Catalytic Activity. *J. Catal.* **2004**, *221*, 335−346.
(50) Lei, Y.-M.; Zhuo, Y.; Guo, M.-L.; Chai, Y.-Q.; Yuan, R. Pore confinement-enhanced electrochemiluminescenceon SnO_2 nanocrystal xerogel with NO_3^- as co-reactant and its application in facile and sensitive bioanalysis. *Anal. Chem.* **2020**, *92*, 2839−2846.
(51) Alfaya, A. A.; Gushikem, Y. The preparation and application of silica−zirconia xerogel as potentiometric sensor for chromium (VI). *J. Colloid Interface Sci.* **1999**, *209*, 428−434.
(52) Pavan, F. A.; Ribeiro, E. S.; Gushikem, Y. Congo red immobilized on a silica/aniline xerogel: Preparation and application as an amperometric sensor for ascorbic acid. *Electroanalysis* **2005**, *17*, 625−629.
(53) Wu, Y.; Xie, Y.; Zhong, F.; Gao, J.; Yao, J. Fabrication of bimetallic Hofmann-type metal-organic frameworks@cellulose aerogels for efficient iodine capture. *Microporous Mesoporous Mater.* **2020**, *306*, No. 110386.
(54) Ebert, W. L.; Cruse, T. A.; X, C.; Gattu, V. K.; Jerden, J. L., Jr. *Status Report on Electrochemical Tests with AgI*, NTRD-MRWFD-2017-000196, 2017.
(55) Asmussen, R. M.; Pearce, C. I.; Lawter, A. R.; Neeway, J. J.; Lawler, B.; Smith, G. L.; Serne, R. J.; Qafoku, N. P.; Miller, B. D.; Swanberg, D. J. *Preparation, Performance and Mechanism of Tc and I Getters in Cementitious Waste Forms*, WM Symposia, Tempe, AZ, USA, 2017.
(56) Bruffey, S. H.; Jubin, R. T.; Jordan, J. A. Capture of elemental and organic iodine from dilute gas streams by silver-exchanged mordenite. *Procedia Chem.* **2016**, *21*, 293−299.
(57) Brunauer, S.; Emmett, P. H.; Teller, E. Adsorption of gases in multimolecular layers. *J. Am. Chem. Soc.* **1938**, *60*, 309−319.
(58) Gregg, S.; Sing, K. *Adsorption, Surface Area, and Porosity*, 2nd ed.; Academic Press: Orlando, 1982.
(59) Cheary, R. W.; Coelho, A. A.; Cline, J. P. Fundamental parameters line profile fitting in laboratory diffractometers. *J. Res. Natl. Inst. Stand. Technol.* **2004**, *109*, 1−25.

https://doi.org/10.1021/acsomega.1c00852
ACS Omega 2021, 6, 11628−11638